Monte Carlo model validation of a detector system used for Positron Emission Particle Tracking

Matthew Herald [a],*, Tzany Wheldon [b,c], Christopher Windows-Yule [a,c]

[a] *School of Chemical Engineering, University of Birmingham, Birmingham, United Kingdom*
[b] *School of Physics and Astronomy, University of Birmingham, Birmingham, United Kingdom*
[c] *Positron Imaging Centre, University of Birmingham, Birmingham, United Kingdom*

ARTICLE INFO

ABSTRACT

The spatiotemporal resolution of Lagrangian particle trajectories captured using Positron Emission Particle Tracking (PEPT) is difficult to predict prior to experimentation, since this relies on the detector systems, source activity distribution, and experimental apparatus. However, understanding the limitations of an experiment is crucial to quantifying error and ensuring that the captured trajectories reveal phenomena of interest in enough detail for meaningful analysis. These factors are especially important in PEPT experiments since this technique is applied to image opaque systems lacking optical access for complementary measurement techniques, such as Particle Image Velocimetry. Using the Monte Carlo simulator Geant4 Application for Tomographic Emission (GATE), a computational model of the ADAC/Phillips Forte, a detector system used at the Positron Imaging Centre (PIC) for PEPT studies, is created and validated against experiments testing the spatial resolution, sensitivity, scatter fraction, and count-rates following National Electronic Manufactures Association standards. In this work, fluorine-18 sources and experimental geometries are recreated, generating synthetic data analogous to experimentally acquired data. Over all experiments and activities tested, this GATE model reports agreement to within 1%–10% of experiments. In the future, this model is expected to be used by the PIC to conduct feasibility studies of potential experiments. Further, optimization of experiments can now be conducted without expending the considerable time and resources required for physical experimentation, representing a major improvement of the PIC's PEPT modeling capabilities.

1. Introduction

Positron Emission Particle Tracking (PEPT) is a technique similar to Positron Emission Tomography (PET) that has been developed to study opaque systems such as rotating drums, fluidized beds, and other industrial equipment without optical access [1]. A positron-emitting substance is bound chemically or physically to a discrete particle, then tracked as a Lagrangian tracer as it moves within a system [2,3]. This technique relies on detecting pairs of annihilation photons emitted by the tracer particle, using these Lines-of-Response (LORs) to successively calculate the position of the tracer [4]. Analysis of trajectories reveals the velocity flow fields, particle residence times, recirculation periods and other time-averaged behavior used in engineering analysis of industrial equipment [5–8] (see Fig. 1).

Using Monte Carlo simulators such as Geant4 Application for Tomographic Emission (GATE), it is possible to model the PET systems on which PEPT experiments are conducted, generating synthetic data analogous to real LORs [9,10] [11]. GATE modeled PET systems such as the Siemens Inveon, Philips Allegro, and the General Electric Discovery report agreement with validation experiments to within 1%–10% in spatial resolution, sensitivity, count-rates, and scatter fraction [12–14]. Additionally, several single-head gamma-cameras such as the Philips AXIS, GEMS DST Xli, and Millennium VG Hawk-Eye have been modeled and validated using GATE [15,16]. These models are useful for iterating through variations of experiments for optimization or testing image reconstruction algorithms without expending the considerable time and resources required for physical experimentation.

In this work, GATE is used to model the ADAC/Phillps Forte, a PET system used for PEPT research at the University of Birmingham Positron Imaging Centre (PIC). The Monte Carlo model is then validated by experiments. While this is an older PET system, no validated GATE models exist to the authors knowledge. Previous to this work, the performance of real experiments has been difficult to predict since there is often a complex experimental geometry, a moving source within the FOV, and a nonlinear response of the detector to the source activity and energy. For future PEPT experiments at the PIC, this model is expected to be used for feasibility studies of proposed PEPT experiments by providing an estimate of the Forte output. Recently, an approach for
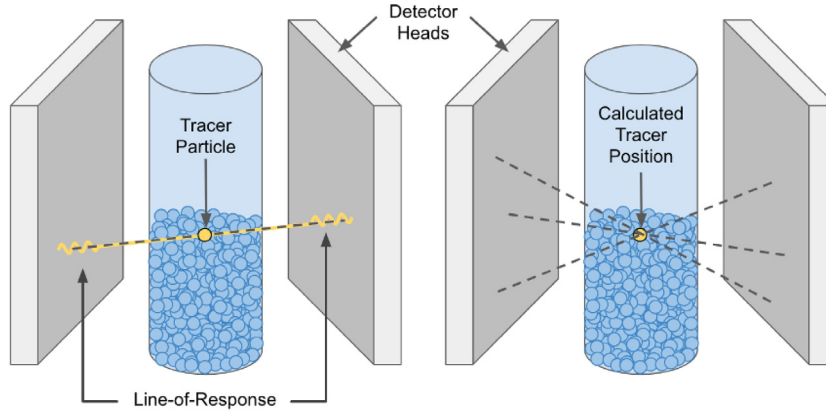
Fig. 1. PEPT locates a positron-emitting tracer in a dense granular system by calculating the intersection of LORs, generated by detecting pairs of annihilation photons.

Fig. 2. The Forte can accommodate large experiments for investigation with PEPT due to its dual-headed geometry. The coordinate system in this work begins in the center of the FOV.

creating virtual PEPT experiments in GATE has been used which integrates tracer trajectory data from simulations with pre-existing GATE models of PET systems [17]. GATE simulations coupled to simulated trajectories produced by multiphysics modeling such as Computational Fluid Dynamics (CFD) or the Discrete Element Method (DEM) may prove especially useful, representing a major improvement in the PIC's PEPT modeling capabilities. The development of an accurate simulation model of the ADAC Forte camera will also provide an invaluable testing ground for the development of new PEPT algorithms (see Fig. 2).

2. Methods

For validating GATE models, a number of approaches have been used in the past, generally relying on standards published by the National Electronics Manufacturers Association (NEMA) [18]. The NEMA standards describe methods for calculating the true, scattered, and random coincidences count-rates, as well as the spatial resolution and sensitivity of PET systems using standard procedures and phantoms. The performance of PET systems following NEMA standards are usually provided by the manufacturer, providing a way for customers to compare the performance of systems in such a way as to not bias one system over the other, providing a guaranteed level of performance.

In this work, experiments testing the spatial resolution, sensitivity, scatter fraction, and count-rates of the Forte are conducted following

Table 1
Positions of the spatial resolution tracer in the Forte FOV.

X-Position (mm)	Y-Position (mm)	Z-Position (mm)
0	0	0
0	127.5	0
0	0	95
150	0	0
150	127.5	0
150	0	95

the NEMA standards for data analysis. All experimental phantoms are replicated in GATE simulations to provide a basis for validation. The Forte has also been characterized in other work to demonstrate improved capabilities, replacing a predecessor system used for PEPT studies at the PIC [19]. This previous characterization provides an important comparison for the results of this work.

2.1. Spatial resolution

Spatial resolution is the ability to distinguish the position of a source within the system field of view (FOV). It is reported as the full-width half-maximum (FWHM) of a source projection created by a back-projection of LORs taken at the source's position. In this work, the axial and transaxial spatial resolution is reported for a small spherical source in air measured in the FOV at locations prescribed by the NEMA protocol. For a coordinate system starting at the central point between the two detector heads separated by 600 mm, the positions of the source used in this experiment are recorded in Table 1.

When calculating the FWHM, 1,000,000 LORs are used to reduce statistical uncertainty. The FWHM of each acquisition is determined by linear interpolation of the projection profile created by single-slice rebinning of the LORs using 1 mm bins.

$$Res_{Transaxial_{Center}} = (Res_{y_{x=0,y=0,z=0}} + Res_{z_{x=0,y=0,z=0}}$$
$$+ Res_{y_{x=0,y=0,z=95}} + Res_{z_{x=0,y=0,z=95}})/4 \qquad (1)$$
$$Res_{Transaxial_{1/2FOV}} = (Res_{y_{x=150,y=127.5,z=0}} + Res_{z_{x=150,y=127.5,z=0}}$$
$$+ Res_{y_{x=0,y=127.5,z=0}} + Res_{z_{x=0,y=127.5,z=0}})/4 \qquad (2)$$
$$Res_{Axial_{Center}} = (Res_{x_{x=0,y=0,z=0}} + Res_{x_{x=0,y=0,z=95}})/2 \qquad (3)$$
$$Res_{Axial_{1/2FOV}} = (Res_{x_{x=150,y=0,z=0}} + Res_{x_{x=150,y=0,z=95}})/2 \qquad (4)$$

The phantom and source used in this experiment is a 0.2 mm diameter anionic exchange resin bead. Anionic exchange beads selectively absorb fluorine-18 ions from a solution of water and fluorine-18, volumetrically activating the bead with a high activity concentration [20]. After soaking in the solution for approximately 30 min, a resin bead was extracted and its activity measured with a well-counter to be
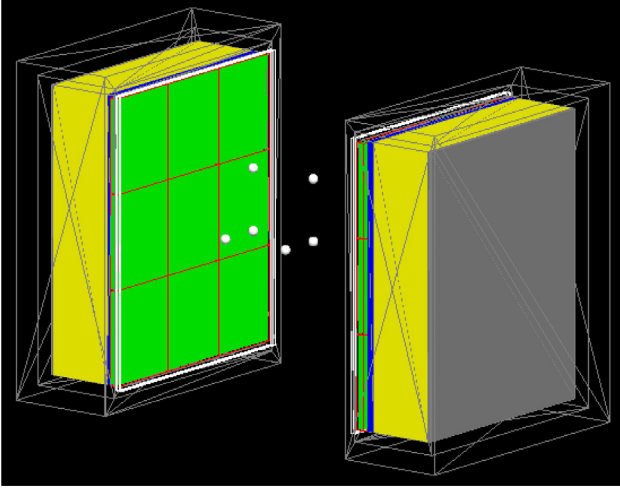
Fig. 3. Locations of the spatial resolution phantom positions, with exaggerated phantom size.

approximately 27.8 MBq ± 0.1. The resin bead was attached to the end of a 1.5 mm diameter stainless-steel syringe using a UV activated epoxy. The syringe was taped to a 200 mm long and 5 mm diameter wooden dowel, then placed in the FOV of the detectors.

A GATE model of the spatial resolution phantom and source has been designed to recreate the experimental geometry. The exact composition of the resin bead is unknown but was modeled as a 0.2 mm diameter spherical plastic source, encapsulated in a spherical plastic phantom 2 mm in diameter. This outer sphere represents the UV activated epoxy and provides material for positrons to annihilate near the source. By the end of the experiments, the source activity decayed to approximately 19 MBq (see Fig. 3).

The source projections are created using the 'Voxels' base-class of the PEPT Library, an open-source Python library of functions useful for analyzing PEPT data [21]. Voxels are the 3D equivalent of 2D pixels. Similar to an image, voxels can be arranged into 3D arrays. In the context of PEPT experiment, the detected LORs are converted into voxel images by finding and increasing the scalar value of the voxels which are crossed by the line. This process can be repeated with successive LORs, creating a array corresponding to the density of LORs and can be visualized by looking at a 2D slice of the 3D voxel array. The line-density is the back-projected image of the source used to fit the FWHM (see Fig. 4).

2.2. Sensitivity

Sensitivity is the rate of detected coincidences compared to the rate of positron-annihilation produced by a source. Geometric and intrinsic factors such as the detector and source positions as well the scintillation crystal material determine the sensitivity of PET systems, however, at high count-rates, the dead-time from electronic pulse processing can restrict the number of events able to be recorded. For low activity sources the rate of detected coincidences, R, is approximately the source activity, A, multiplied by the geometric efficiency, ε_g, and multiplied by the square of the intrinsic efficiency, ε_i, since both coincident photons must be detected. The intrinsic efficiency should remain relatively constant for these experiments but has some dependency on the head separation and source position due to the depth of photon interaction [22].

$$R = A\varepsilon_g \varepsilon_i^2 \tag{5}$$

For a centrally located point source in between the two detector heads separated by a distance S, the geometric efficiency can be defined as the solid angle between the point source and limits of the

detector, length L and height H. The geometric efficiency of the Forte was studied in previous work and an analytical expression derived to calculate the geometric efficiency for an ideal point source anywhere in the FOV [23]. This expression transforms the Cartesian coordinates into spherical coordinates and integrates across the zenith, ϕ, and azimuth, θ. Using trigonometric identities, the geometric efficiency can be expressed solely by integrating the azimuth angle.

$$d\varepsilon_g = \frac{\sin\phi \, d\theta \, d\phi}{2\pi} \tag{6}$$

$$\theta_{min} = \arctan\left(\max\left\{\frac{S-2x}{L-2z}; \frac{S+2x}{L+2z}\right\}\right) \tag{7}$$

$$\theta_{max} = \pi - \arctan\left(\max\left\{\frac{S-2x}{L+2z}; \frac{S+2x}{L-2z}\right\}\right) \tag{8}$$

$$\varepsilon_g = \frac{1}{2\pi}\sum_{q=1}^{2}\int_{\theta_{min}}^{\theta_{max}} (\max\left\{\frac{S-2x}{H+(-1)^q 2y}; \frac{S+2x}{H-(-1)^q 2y}\right\}^2 \csc^2\theta + 1)^{-\frac{1}{2}} d\theta$$

$$\tag{9}$$

For the Forte, the detector area is 380 mm in length and 510 mm in height, resulting in a geometric efficiency of approximately 12% for a head separation of 600 mm. Sensitivity is highest in the center of the field of view and decreases rapidly as the source moves off-axis. Additionally, by sampling the geometric efficiency at several points within the FOV and multiplying by the square of the intrinsic efficiency, a sensitivity field can be created and visualized (see Fig. 5).

In this work, a directly activated 2 mm glass bead attached to the end of a long stainless-steel syringe is placed in the center of the FOV with a detector separation of 600 mm. Since positrons emitted from fluorine-18 can have a considerable range in air, the peak sensitivity is found by removing successive layers of shielding from the point source. The shielding provides material for positrons to annihilate with an electron, then the expected counts for a bare source in air are found by extrapolating the shielded count-rates. The parameters C_1 and C_2 are fitted, so as long as the shielding is of uniform material the attenuation coefficient is not needed.

$$R = C_1 e^{-C_2 t} \tag{10}$$

The activity of the source in these experiments is measured by a well-counter to be 10.5 MBq ± 0.1, decaying to approximately 8 MBq when the last shield is placed over the source. The shields are four 150 mm long, 0.75 mm thick stainless-steel tubes of increasing diameter placed over the point source. For each measurement 1,000,000 LORs are used to reduce statistical uncertainty. Using a value of 24% for the intrinsic efficiency the expected sensitivity of the Forte at 600 mm is 6.49 kHz/MBq.

2.3. Scatter fraction and count-rates

All LORs acquired by PET systems are either true, scattered or random. The scatter fraction is the fraction of detected coincidences in which one or both rays undergo scattering. This corrupts the LORs, since they no longer pass through the point of positron-annihilation. As the experimental system of interest becomes denser, more rays are scattered, reducing the maximum achievable true LOR count-rate. In addition to scattered coincidences, two unrelated events can be detected and associated as a coincidence if they occur within the coincidence window. At high count-rates, random LORs can constitute a large fraction of the total LORs since they scale with the square of the singles rate, S [24].

$$R_{Total} = R_{True} + R_{Scattered} + R_{Random} \tag{11}$$

$$R_{Random} = 2\tau S^2 \tag{12}$$

To measure the scatter fraction, the scattered LORs must be extracted from the true and random LORs. NEMA describes an experiment using a line source inserted into a high-density polyethylene (HDPE) phantom as the basis for calculating the scatter fraction and count-rates.
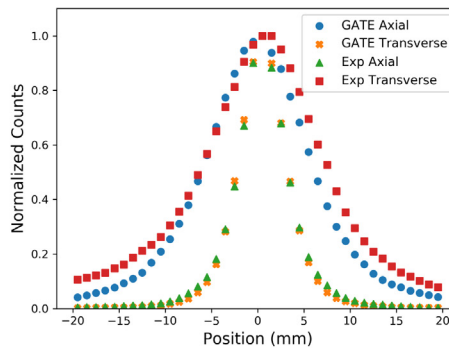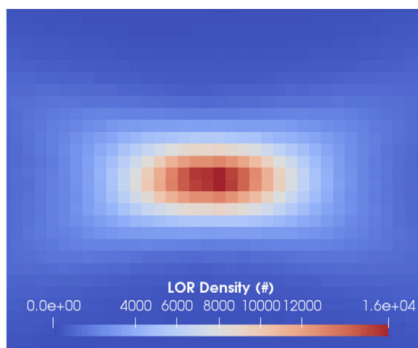
Fig. 4. Left: 2D slice of the 3D voxel array for a source near the center of the FOV. Both the Axial and Transaxial spatial resolutions are visible. Each voxel edge is 1 mm. Right: 1D back-projection of the experimental and GATE simulated spatial resolution phantom at the central position of the Forte FOV.
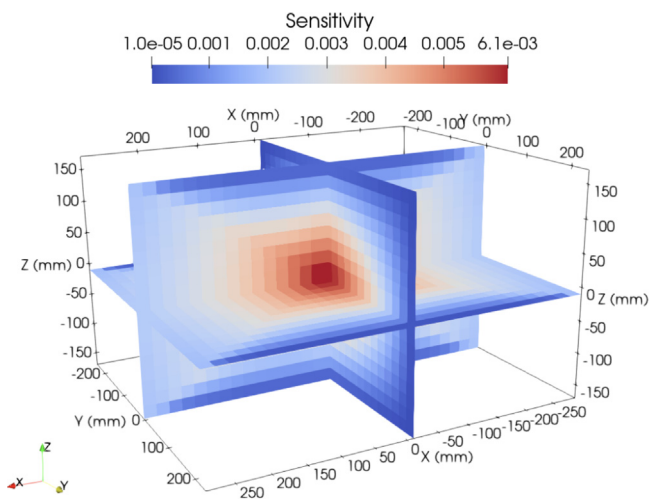

Fig. 5. 3D Total Sensitivity field of the Forte at a head separation of 600 mm.

However, due to the unavailability of specialized NEMA compliant phantoms, other phantoms are used in their place. As reported by others, the non-standard phantoms can be used in place of NEMA phantoms with little effect on the overall results [25,26]. For the purposes of this work, any phantom could be used, since the objective is to create a validated GATE model, as opposed to a performing quality assessment of the Forte. A smaller cylindrical HDPE phantom is used in this work and the NEMA methods applied. This phantom has an outside diameter of 50 mm and length 120 mm, with an internal cylindrical cavity of diameter 10 mm and length 100 mm. The phantom is filled with approximately 100 MBq of fluorine-18 well-mixed with water at the start of the experiment then imaged over several half-lives. The head separation is set to 445 mm.

When imaging this source using single-slice rebinning, the true, scattered, and random LORs can be isolated by following the NEMA protocol. The true LORs are all contained within the 40 mm strip centered on the maximum pixel with all other counts outside this strip being scattered or random. To remove scattered and random counts within the 40 mm strip, the pixel intensities on the edges of this strip are linearly interpolated and subtracted, leaving only the true LORs. The random LORs can be further extracted using a random coincidence estimate, however, for simplicity, the scatter fraction in this work is reported as the ratio of scattered and random LORs acquired during the lowest activity run. In this way, the random contribution is minimal.

$$R_{Scatter} = R_{Total} - R_{True} \tag{13}$$

$$SF = R_{Scatter}/R_{Total} \tag{14}$$

In addition to the true, scattered, and random count-rates, the Noise Equivalent count-rate (NEC) is computed as the square of the true counts divided by the total number of counts. The NEC has little relationship to actual noise, but rather provides a measure of relative count-rate contributions from true, scattered, and random coincidences. It is commonly used as a figure of merit for comparing PET systems [27].

$$NEC = R_{True}^2/R_{Total} \tag{15}$$

2.4. GATE model

GATE is a Monte Carlo simulator based on Geant4 libraries, designed for the simulation of PET scanners and other medical imaging devices [28]. The geometry of detectors and experiments can be created using simple shapes or geometries imported from mesh files, meaning a wide range of systems can be modeled. Further, the affects of signal-processing can be emulated using GATE, including the energy resolution of scintillation crystals, energy windows for accepting events, coincidence timing windows, time-resolution of recorded events, and dead-time of the PMTs. Accurate modeling of signal-processing is crucial for replicating realistic detector response over a wide-range of activities since the energy response and count-rates in real systems are greatly affected by these processes [29].

In this work, the geometric model of the Forte is informed by design drawings provided by the manufacturer, measurements taken at the PIC. The Forte possesses a wide-area NaI scintillation crystal of dimensions 590 x 470 x 16 mm, optically coupled to a glass light-guide. This component is considered the sensitive detector in the GATE simulation, the volume in which events are detected. Additionally, an aluminum gantry ring, aluminum casing around the detector heads, and lead shielding are added since these components will contribute significantly to the overall scatter. Further add to the geometric model, a generalized back-compartment corresponding to the 'intermediate complexity' back-compartment described by Rault et al. is added to account for scattering within the PMTs and internal electronics [30]. An accurate back-compartment is needed when modeling photons over 300 keV since these rays can pass through the relatively thin scintillation crystal and back-scatter, contaminating the energy spectrum (see Fig. 6)

The signal-processing of the Forte, referred to as the digitizer, is informed by previously published work using the Forte and experiments conducted in this work [19]. The energy resolution is reported to be approximately 14% at 511 keV for moderate count-rates. When used for PEPT, a 50% energy window of 350–650 keV is applied to discard the majority of scattered rays, while maintaining high coincidence rates. The detector is operated in coincidence with a window of 15 ns and reported time resolution of 15 ns. Additionally, only pulses from the central 510 x 380 mm area of the detector crystal are accepted. When the pulses falling outside this range are rejected for a central point
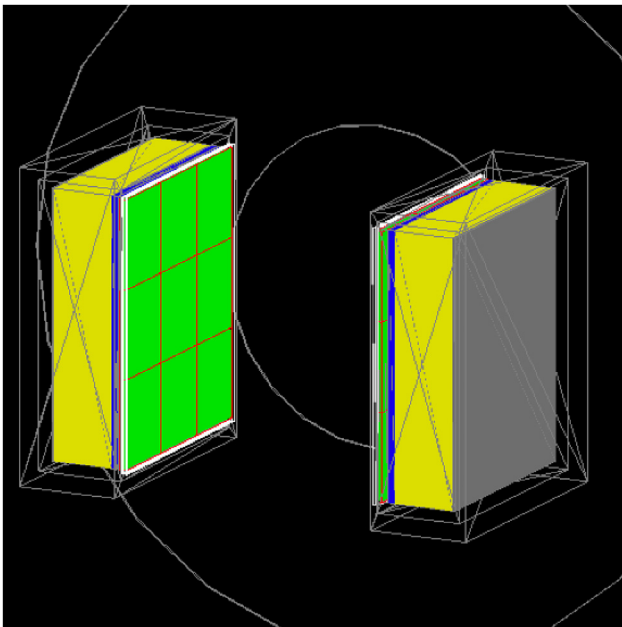
Fig. 6. GATE model of the Forte. NaI crystal (green, red outline), glass lightguide (blue), PMTs (yellow), electronics (gray), Al casing and Pb shielding (gray box outline), Al ring (gray ring outline), plastic front cover (white outline). (For interpretation of the references to color in this figure legend, the reader is referred to the web version of this article.)

Table 2
Forte geometry description.

Geometric Model	Values
Detector dimensions	590 × 470 × 16 mm
Useful detector area	510 × 380 mm
Dual-Head separation	250–800 mm
Detector crystal	Sodium Iodide
Number of pixels	9

Table 3
Forte digitizer description.

Digitizer model	Values
Coincidence window	15 ns
Time resolution	15 ns
Paralyzable Dead-Time per pixel	1.15 μs
Non-Paralyzable Dead-Time	1.15 μs
Energy resolution at 511 keV	14%
Energy window	350–650 keV (50% Photopeak)
Intrinsic efficiency	24%

Table 4
Experimental and simulated phantom characteristics.

Characteristic	Spatial resolution	Sensitivity	Scatter and Count-Rates
Material	Resin, Plastic, Stainless-steel, Wood	Glass, Stainless-steel	HDPE, Water
Dimensions	0.2 mm diameter resin bead, 1.5 mm diameter syringe, dowel 200 mm length	2 mm diameter bead, 0.75 mm thickness shield, 150 mm length	120 mm height, 50 mm diameter, 12 mm inner diameter, 100 mm inner height
Head Separation	600 mm	600 mm	445 mm
Initial Activity	27.8 MBq	10 MBq	100 MBq

source, the count-rate is reduced by 20%–30%, determined by the geometric efficiency. This effect is added in post-processing of the GATE generated LORs by rejecting LORs falling outside the active area.

Another consideration for the GATE model is the amount of spatial blurring to apply to the detected LORs. This blurring refers to an applied random movement in each position component of the detected LOR. The fluctuation in position follows a normal distribution with an FWHM set by the user. GATE simulation results will generally report a better spatial resolution than experimental measurements if spatial blurring is not simulated [31]. To investigate this effect, an additional series of simulations are conducted with the spatial blurring module activated in the digitizer. It is unknown how much additional spatial blurring is needed to recreate experimental results, so 3, 5, and 7 mm blurring are investigated and the best fit to experimental data is selected.

Additionally, the digitizer settings are crucial for accurate dead-time emulation. When a photon interaction triggers detector to convert the light generated by the scintillation crystal into an electronic pulse, dead-time occurs during which the detector is unable to accept a new pulse and other pulses may 'pile-up', being detected as a single pulse or simply lost [32]. A wide range of models have been proposed to account for this effect in PET systems including paralyzable, non-paralyzable, and hybrid models [33]. These models refer to the behavior of the dead-time, describing whether new pulses occurring during the dead-time extend the dead-time (paralyzable), do not extend the dead-time (non-paralyzable), or cause some mixture of the two behaviors (hybrid). The dead-time of the Forte is considered to have a hybrid dead-time, since each pixel is paralyzable, however, the recording of LORs is a non-paralyzable process.

Complicating the addition of dead-time in this GATE model is the need to account for the pseudo-independent zones of the scintillation crystal. When a scintillation event occurs, approximately only 6–7 individual photomultiplier tubes are activated out of an array of 55 on each head. The position of photon interaction is then calculated as the energy-centroid of the light collected by these PMTs, referred to as Anger logic [34]. To model these pseudo-independent zones, in

lieu of not applying Anger logic directly, 9 pixels are used, arranged in a 3 × 3 array, since this the closest approximation of the area covering 6–7 PMTs. The dead-time per pixel is determined to be 1.15 μs by fitting the GATE produced count-rate curves to previously published data and an independent count-rate experiment conducted in this work [19]. This value disagrees with the published value of 170 ns for the non-paralyzable model described by Parker et al. but is closer to the manufacturer specification 1.3 μs, though it is not known how the manufacturer's value was derived. The non-paralyzable dead-time is also set to 1.15 μs (see Tables 2 and 3).

Next, the phantom and source geometries must be described. Three geometries are used for these experiments: an activated resin bead, coated in epoxy on the end of a hollow stainless-steel syringe, stainless steel cylinders placed over the point source, and a high-density polyethylene (HDPE) cylinder filled with water well-mixed with fluorine-18. These are the spatial resolution phantom, sensitivity phantom, and scatter fraction phantom, respectively. These phantoms are described in detail in the sections above (see Fig. 7, Table 4).

3. Results

3.1. Spatial resolution

The experimental spatial resolution phantom in the center of the FOV of the Forte produces a central axial FWHM of 16.28 mm and transaxial FWHM of 5.39 mm. The spatial resolution was also measured at 1/2 FOV. The 1/2 FOV axial and transaxial FWHM are measured to be 19.62 mm and 5.13, respectively. Compared to the experiment, the GATE simulation without spatial blurring underpredicts the FWHM
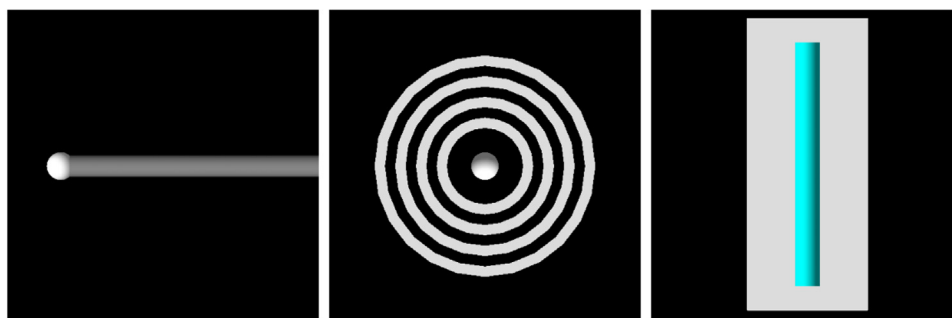
Fig. 7. The side view of the spatial resolution phantom (left), top down view of the sensitivity phantom (center), and cut-away view of the scatter fraction and count-rates phantom (right).
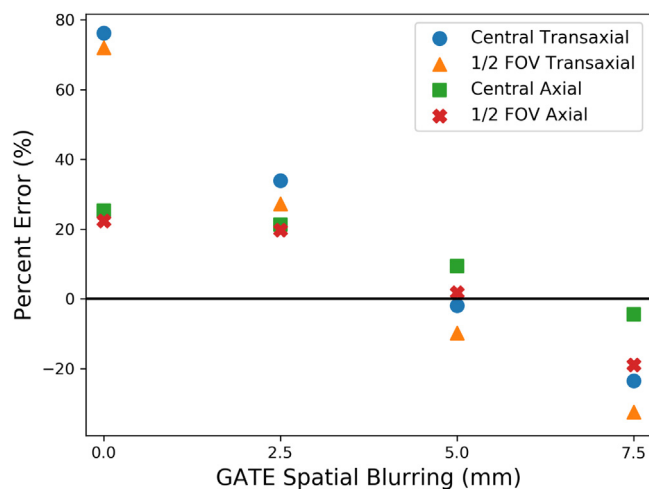

Fig. 8. The amount of spatial blurring applied to the GATE simulated LORs was varied and compared to the experimentally determined spatial resolution of the Forte.

Fig. 9. Measured and extrapolated counts of the sensitivity experiment, showing close agreement when shielding is present and poor agreement for a bare source.

in both the axial and axial directions, indicating that spatial blurring is required. The 2.5, 5, and 7.5 mm spatial blurring simulations were compared, with the 5 mm blurring GATE simulation agreeing best with the experiment, though still under-predicting the transaxial FWHM. In previous work, the Forte was measured to have an transaxial spatial resolution of approximately 6 mm by fitting 1D a Gaussian function to a point source profile in air [19]. The measurements in this work vary, but are consistent with this value (see Fig. 8, Table 5).

3.2. Sensitivity

Comparing the results of the sensitivity experiment, the experimental sensitivity of the Forte is measured to be approximately 6.76 kHz/MBq, whereas the simulated sensitivity is reported to be 6.42 kHz/MBq. This translates into a −5.03% error between the experiment and simulation. The predicted theoretical sensitivity based on the geometric and intrinsic efficiencies, is approximately 6.49 kHz/MBq, showing agreement between theory, experiment, and simulation (see Fig. 9).

Further, the linear attenuation coefficient of the shielding in the experiment, calculated by fitting the count-rates, is 0.105 mm^{-1} compared to simulated value of 0.097 mm^{-1}, representing a −7.62% error. When the shielding is present the experiment and simulation agree well, however, when the source is imaged without shielding, the count-rates between the experiment and simulate vary significantly. This discrepancy is addressed in the discussion section.
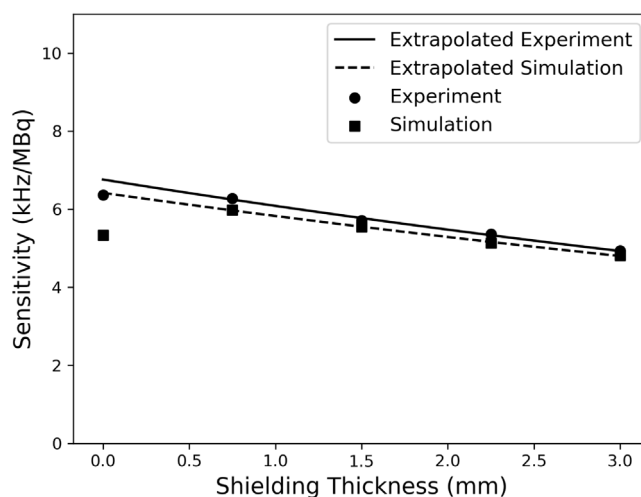
Table 5
Experimental and simulated spatial resolution results.

Spatial resolution	Experiment	0 mm Blurring	5 mm Blurring
Central axial (mm)	14.680	10.965	13.294
Central transaxial (mm)	5.567	3.159	5.675
1/2 FOV axial (mm)	17.217	13.368	16.904
1/2 FOV transaxial (mm)	4.941	2.871	5.477

3.3. Scatter fraction and count-rates

The scatter fraction of the experiment and simulation in the lowest activity acquisition show relatively good agreement, however the experiment reports a slightly higher scatter fraction than the simulation. The experimental measured scatter fraction is approximately 0.167, compared to the simulated value of approximately 0.155, representing a −7.19% error. Over 1–100 MBq, simulated scatter and random fraction continue to agree, though at high source activities the scattered plus random and true fraction begin to diverge, with a maximum error of −14.21% at 100 MBq, possible reasons for this are covered in the discussion (see Fig. 10).

Further, the results of the count-rate experiment and simulation are in good agreement, with the total, true, scattered plus random, and NEC count-rates differing by less than 10% over the range of 1–100 MBq. The total and true count-rates perform particularly well, with an average error of 2.87% and 6.04%, respectively over the range of tested activities. The peak true coincidence rate of the experiment is
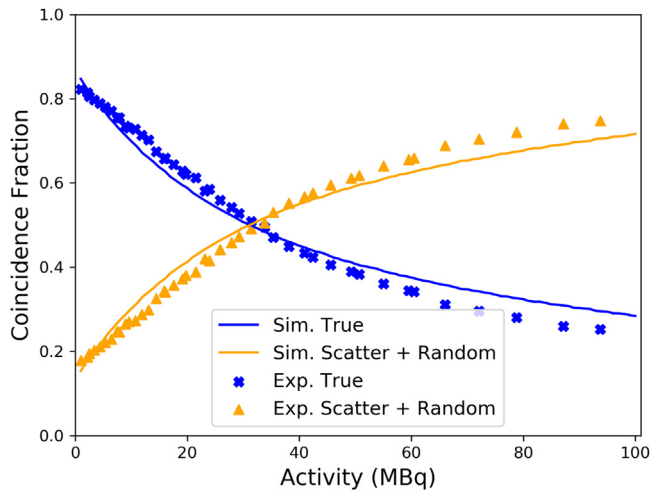
Fig. 10. The true LORs and scattered plus random LORs for the simulation and experiments.
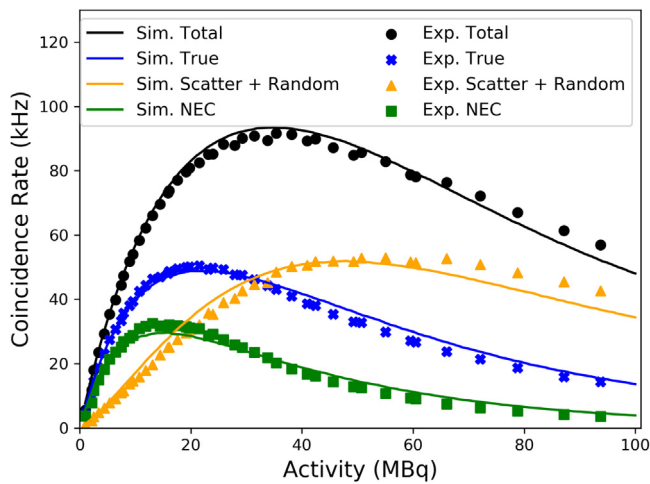

Fig. 11. Results of the count-rate experiment with the total (black), true (blue), scattered plus random (orange), and NEC (green) rates for both the experiment and simulation. (For interpretation of the references to color in this figure legend, the reader is referred to the web version of this article.)

Table 6
Results from the validation experiments conducted in this work.

Validation characteristic	Percent error (%)	Count-Rate	Absolute percent error (%)
Central axial	9.44	–	–
Central transaxial	−1.90	–	–
1/2 FOV axial	1.82	Total	2.87
1/2 FOV transaxial	−9.79	True	4.59
Sensitivity	−5.03	Corrupted	8.08
Scatter fraction	−7.19	NEC	10.18

coefficient of the stainless-steel shielding. In previous work using the Forte, intrinsic efficiency is reported to be 23%, though a value of 24% appears to match this work better. While the theoretical, experimental, and simulated sensitivity are in good agreement, the counts for the unshielded source in the simulation do not agree, introducing a discrepancy. One reason for this could be differences in the air definition of the simulation compared to the actual conditions on the day of the experiment. The range of positrons emitted in diffuse media, such as air, can travel considerable distances before annihilating with an electron [35]. The density of air in GATE is 1.29 kg/m^3, however, the density of air is sensitive to both temperature and humidity which can affect the positron range. This is likely the source of error for this case, but differences between the source geometry or activity in the simulation could also be responsible.

The scatter fraction and count-rate experiment and simulation at low count-rates are at low and moderate activities are in good agreement, demonstrating that the source and geometric definitions are accurate since these are main contributors to the count-rates in these cases. At high activities the scattered and random counts diverge, with a maximum error of −14.21% at 100 MBq, which could indicate inaccuracies in the digitizer model or the pixelated detector crystal. Since crosstalk between the crystals or afterglow caused by defective crystals are not explicitly simulated, at high count rates these effects may introduce excessive error in positioning the point of interaction of photons [36]. This could explain why the total count-rate remains accurate, while the scatter and random count-rate is higher in the experiment than the simulation. However, this discrepancy is not significant since PEPT experiments using the Forte rarely use source activities where this would become an issue.

5. Conclusions

In this work, three experiments were conducted to validate a GATE model of the Forte, testing the spatial resolution, sensitivity, the scatter fraction, and count-rates. Overall, this GATE model agrees with experiment to within approximately 10% over all experiments and activities, consistent with values reported of other systems modeled using GATE (see Table 6).

Spatial resolution, sensitivity, scatter fraction, and count-rates are characteristics of interest in predicting the performance of PEPT experiments. By using realistic phantoms descriptions, this model has been shown to generate synthetic LORs from replicated experimental conditions. This is useful since a balance between the quantity and quality of LORs is desired in PEPT experiments. High count-rates are needed to create sufficient temporal resolution or tracers along their trajectory, however, increasing the source activity can result in poor count-rates due to excessive dead-time. Additionally, the fraction of corrupted events also increases at high count-rates, degrading spatial resolution of reconstructed trajectories.

Combined with the DEM simulation capabilities of the PIC, this GATE model has the potential to resolve several outstanding questions pertaining to the optimization of PEPT experiments. What is the source activity for a given experiment that will return the highest true LOR count-rates? How much material can annihilation photons

50.3 kHz at 21.4 MBq compared to the simulated values of 48.5 kHz at 21.4 MBq. Additionally, the peak experimental NEC rate of 32.1 kHz occurs at 13.2 MBq compared to the simulated values of 29.6 kHz at 14.2 MBq, showing close agreement (see Fig. 11).

4. Discussion

The spatial resolution of the GATE simulation without added spatial blurring is considerably higher than what was measured in the experiment, demonstrating that the spatial blurring module is needed to degrade the resolution of detected LORs in order to match the experimental data. Accurate replication of the spatial resolution is important for simulating PEPT experiments since it will affect the fidelity of reconstructed trajectories, distorting the tracked position of source and can introduce spurious tracer velocities. For the Forte, approximately 5 mm of spatial blurring is required at activities around 20 MBq. It is expected that at lower activities the amount of spatial blurring can be decreased, but more experiments are needed to confirm this.

The sensitivity simulation agrees with experiment in both the overall sensitivity of Forte, as well as the calculated linear attenuation

penetrate without being excessively corrupted by scattering? Can the spatiotemporal resolution of trajectories be improved by changing the detector geometry or digitizer settings? These questions can now be systematically investigated using Monte Carlo simulations without expending considerable time using the Forte, which is often constantly in use by researchers and companies conducting PEPT experiments. For proposed experiments, this model can also be used for feasibility studies, ensuring that the expected tracer velocities can be tracked or that the experimental apparatus will not introduce excessive scattering, representing a major improvement in PEPT modeling by the PIC.

CRediT authorship contribution statement

Matthew Herald: Conceptualization, Methodology, Software, Validation, Formal analysis, Investigation, Data curation management, Writing - original draft, Visualization. **Christopher Windows-Yule:** Conceptualization, Writing - review & editing, Supervision.

Declaration of competing interest

The authors declare that they have no known competing financial interests or personal relationships that could have appeared to influence the work reported in this paper.

Acknowledgment

References

[1] D.J. Parker, Positron emission particle tracking and its application to granular media, Rev. Sci. Instrum. 88 (5) (2017) 051803, http://dx.doi.org/10.1063/1.4983046, URL: http://aip.scitation.org/doi/10.1063/1.4983046.

[2] R. Shaw, Signalling particles for introduction into blood flowing through a vessel of interest, 1978, URL: https://patents.google.com/patent/US4224303A/en.

[3] M. Hawkesworth, D. Parker, P. Fowles, J. Crilly, N. Jefferies, G. Jonkers, Nonmedical applications of a positron camera, Nucl. Instrum. Methods Phys. Res. A 310 (1–2) (1991) 423–434, http://dx.doi.org/10.1016/0168-9002(91)91073-5, URL: https://linkinghub.elsevier.com/retrieve/pii/0168900291910735.

[4] D. Parker, C. Broadbent, P. Fowles, M. Hawkesworth, P. McNeil, Positron emission particle tracking - a technique for studying flow within engineering equipment, Nucl. Instrum. Methods Phys. Res. A 326 (3) (1993) 592–607, http://dx.doi.org/10.1016/0168-9002(93)90864-E, URL: https://linkinghub.elsevier.com/retrieve/pii/016890029390864E.

[5] R.D. Wildman, J.M. Huntley, D.J. Parker, Convection in highly fluidized three-dimensional granular beds, Phys. Rev. Lett. 86 (15) (2001) 3304–3307, http://dx.doi.org/10.1103/PhysRevLett.86.3304, URL: https://link.aps.org/doi/10.1103/PhysRevLett.86.3304.

[6] R. Pérez-Mohedano, N. Letzelter, C. Amador, C. VanderRoest, S. Bakalis, Positron Emission Particle Tracking (PEPT) for the analysis of water motion in a domestic dishwasher, Chem. Eng. J. 259 (2015) 724–736, http://dx.doi.org/10.1016/j.cej.2014.08.033, URL: https://linkinghub.elsevier.com/retrieve/pii/S1385894714010870.

[7] S. Langford, C. Wiggins, D. Tenpenny, A. Ruggles, Positron emission particle tracking (PEPT) for fluid flow measurements, Nucl. Eng. Des. 302 (2016) 81–89, http://dx.doi.org/10.1016/j.nucengdes.2016.01.017, URL: https://linkinghub.elsevier.com/retrieve/pii/S0029549316000273.

[8] C. Windows-Yule, J. Seville, A. Ingram, D. Parker, Positron emission particle tracking of granular flows, Annu. Rev. Chem. Biomol. Eng. 11 (1) (2020) annurev–chembioeng–011620–120633, http://dx.doi.org/10.1146/annurev-chembioeng-011620-120633, URL: https://www.annualreviews.org/doi/10.1146/annurev-chembioeng-011620-120633.

[9] G. Santin, D. Strul, D. Lazaro, L. Simon, M. Krieguer, M. Martins, V. Breton, C. Morel, GATE: A Geant4-based simulation platform for PET and SPECT integrating movement and time management, IEEE Trans. Nucl. Sci. 50 (5) (2003) 1516–1521, http://dx.doi.org/10.1109/TNS.2003.817974, URL: http://ieeexplore.ieee.org/document/1236960/.

[10] S. Jan, G. Santin, D. Strul, S. Staelens, K. Assié, D. Autret, S. Avner, R. Barbier, M. Bardiès, P.M. Bloomfield, D. Brasse, V. Breton, P. Bruyndonckx, I. Buvat, A.F. Chatziioannou, Y. Choi, Y.H. Chung, C. Comtat, D. Donnarieix, L. Ferrer, S.J. Glick, C.J. Groiselle, D. Guez, P.-F. Honore, S. Kerhoas-Cavata, A.S. Kirov, V. Kohli, M. Koole, M. Krieguer, D.J. van der Laan, F. Lamare, G. Largeron, C. Lartizien, D. Lazaro, M.C. Maas, L. Maigne, F. Mayet, F. Melot, C. Merheb, E. Pennacchio, J. Perez, U. Pietrzyk, F.R. Rannou, M. Rey, D.R. Schaart, C.R. Schmidtlein, L. Simon, T.Y. Song, J.-M. Vieira, D. Visvikis, R. Van de Walle, E. Wieërs, C. Morel, GATE - Geant4 Application for Tomographic Emission: a simulation toolkit for PET and SPECT, Phys. Med. Biol. 49 (19) (2004) 4543–4561, URL: https://www.ncbi.nlm.nih.gov/pmc/articles/PMC3267383/.

[11] S. Jan, G. Santin, D. Strul, S. Staelens, K. Assié, D. Autret, S. Avner, R. Barbier, M. Bardiès, P.M. Bloomfield, D. Brasse, V. Breton, P. Bruyndonckx, I. Buvat, A.F. Chatziioannou, Y. Choi, Y.H. Chung, C. Comtat, D. Donnarieix, L. Ferrer, S.J. Glick, C.J. Groiselle, D. Guez, P.-F. Honore, S. Kerhoas-Cavata, A.S. Kirov, V. Kohli, M. Koole, M. Krieguer, D.J.v.d. Laan, F. Lamare, G. Largeron, C. Lartizien, D. Lazaro, M.C. Maas, L. Maigne, F. Mayet, F. Melot, C. Merheb, E. Pennacchio, J. Perez, U. Pietrzyk, F.R. Rannou, M. Rey, D.R. Schaart, C.R. Schmidtlein, L. Simon, T.Y. Song, J.-M. Vieira, D. Visvikis, R.V.d. Walle, E. Wieërs, C. Morel, GATE: a simulation toolkit for PET and SPECT, Phys. Med. Biol. 49 (19) (2004) 4543–4561, http://dx.doi.org/10.1088/0031-9155/49/19/007, URL: https://iopscience.iop.org/article/10.1088/0031-9155/49/19/007.

[12] S. Lee, J. Gregor, D. Osborne, Development and validation of a complete GATE model of the Siemens Inveon trimodal imaging platform, Mol. Imag. 12 (7) (2013) http://dx.doi.org/10.2310/7290.2013.00058, URL: http://journals.sagepub.com/doi/10.2310/7290.2013.00058, 7290.2013.00058.

[13] F. Lamare, A. Turzo, Y. Bizais, C.C.L. Rest, D. Visvikis, Validation of a Monte Carlo simulation of the Philips Allegro/GEMINI PET systems using GATE, Phys. Med. Biol. 51 (4) (2006) 943–962, http://dx.doi.org/10.1088/0031-9155/51/4/013, URL: https://iopscience.iop.org/article/10.1088/0031-9155/51/4/013.

[14] C.R. Schmidtlein, A.S. Kirov, S.A. Nehmeh, Y.E. Erdi, J.L. Humm, H.I. Amols, L.M. Bidaut, A. Ganin, C.W. Stearns, D.L. McDaniel, K.A. Hamacher, Validation of GATE Monte Carlo simulations of the GE Advance/Discovery LS PET scanners: Validation of GATE simulations of GE PET scanners, Med. Phys. 33 (1) (2005) 198–208, http://dx.doi.org/10.1118/1.2089447, URL: http://doi.wiley.com/10.1118/1.2089447.

[15] S. Staelens, D. Strul, G. Santin, S. Vandenberghe, M. Koole, Y.D. Asseler, I. Lemahieu, R.V.d. Walle, Monte Carlo simulations of a scintillation camera using GATE: validation and application modelling, Phys. Med. Biol. 48 (18) (2003) 3021–3042, http://dx.doi.org/10.1088/0031-9155/48/18/305, URL: https://iopscience.iop.org/article/10.1088/0031-9155/48/18/305.

[16] D. Autret, A. Bitar, L. Ferrer, A. Lisbona, M. Bardiès, Monte Carlo modeling of gamma cameras for I-131 imaging in targeted radiotherapy, Cancer Biother. Radiopharmaceuticals 20 (1) (2005) 77–84, http://dx.doi.org/10.1089/cbr.2005.20.77, URL: http://www.liebertpub.com/doi/10.1089/cbr.2005.20.77.

[17] M. Herald, Z. Bingham, R. Santos, A. Ruggles, Simulated time-dependent data to estimate uncertainty in fluid flow measurements, Nucl. Eng. Des. 337 (2018) 221–227, http://dx.doi.org/10.1016/j.nucengdes.2018.07.005, URL: https://linkinghub.elsevier.com/retrieve/pii/S0029549318303844.

[18] Performance Measurements of Positron Emission Tomographs, Technical Report NU-2-2007, National Electronics Manufacturer Association, 2007.

[19] D. Parker, R. Forster, P. Fowles, P. Takhar, Positron emission particle tracking using the new Birmingham positron camera, Nucl. Instrum. Methods Phys. Res. A 477 (1–3) (2002) 540–545, http://dx.doi.org/10.1016/S0168-9002(01)01919-2, URL: https://linkinghub.elsevier.com/retrieve/pii/S0168900201019192.

[20] X. Fan, D. Parker, M. Smith, Labelling a single particle for positron emission particle tracking using direct activation and ion-exchange techniques, Nucl. Instrum. Methods Phys. Res. A 562 (1) (2006) 345–350, http://dx.doi.org/10.1016/j.nima.2006.03.015.

[21] A.L. Nicuşan, C.R.K. Windows-Yule, Positron emission particle tracking using machine learning, Rev. Sci. Instrum. 91 (1) (2020) 013329, http://dx.doi.org/10.1063/1.5129251.

[22] S. Ahmadi, S. Ashrafi, F. Yazdansetad, A method to calculate the gamma ray detection efficiency of a cylindrical NaI (Tl) crystal, J. Instrum. 13 (05) (2018) P05019, http://dx.doi.org/10.1088/1748-0221/13/05/P05019, URL: https://iopscience.iop.org/article/10.1088/1748-0221/13/05/P05019.

[23] A. Guida, Positron Emission Particle Tracking Applied to Solid-Liquid Mixing in Mechanically Agitated Vessels (Ph.D. thesis), University of Birmingham, 2010, URL: https://etheses.bham.ac.uk/id/eprint/935/.

[24] C. Stearns, D. McDaniel, S. Kohlmyer, P. Arul, B. Geiser, V. Shanmugam, Random coincidence estimation from single event rates on the Discovery ST PET/CT scanner, in: 2003 IEEE Nuclear Science Symposium. Conference Record (IEEE Cat. No.03CH37515), IEEE, Portland, OR, USA, 2004, pp. 3067–3069, http://dx.doi.org/10.1109/NSSMIC.2003.1352545, URL: http://ieeexplore.ieee.org/document/1352545/.

[25] H.W. de Jong, M. Lubberink, H. Watabe, H. Iida, A.A. Lammertsma, A method to measure PET scatter fractions for daily quality control: SF measurement method for daily QC, Med. Phys. 36 (10) (2009) 4609–4615, http://dx.doi.org/10.1118/1.3213096, URL: http://doi.wiley.com/10.1118/1.3213096.

[26] W. Kunze, M. Baehre, E. Richter, PET with a dual-head coincidence camera: spatial resolution, scatter fraction, and sensitivity., J. Nucl. Med. 41 (6) (2000) 1067–1074.

[27] S. Strother, M. Casey, E. Hoffman, Measuring PET scanner sensitivity: relating countrates to image signal-to-noise ratios using noise equivalents counts, IEEE Trans. Nucl. Sci. 37 (2) (1990) 783–788, http://dx.doi.org/10.1109/23.106715, URL: http://ieeexplore.ieee.org/document/106715/.

[28] S. Agostinelli, J. Allison, K. Amako, J. Apostolakis, H. Araujo, P. Arce, M. Asai, D. Axen, S. Banerjee, G. Barrand, F. Behner, L. Bellagamba, J. Boudreau, L. Broglia, A. Brunengo, H. Burkhardt, S. Chauvie, J. Chuma, R. Chytracek, G. Cooperman, G. Cosmo, P. Degtyarenko, A. Dell'Acqua, G. Depaola, D. Dietrich, R. Enami, A. Feliciello, C. Ferguson, H. Fesefeldt, G. Folger, F. Foppiano, A. Forti, S. Garelli, S. Giani, R. Giannitrapani, D. Gibin, J. Gómez Cadenas, I. González, G. Gracia Abril, G. Greeniaus, W. Greiner, V. Grichine, A. Grossheim, S. Guatelli, P. Gumplinger, R. Hamatsu, K. Hashimoto, H. Hasui, A. Heikkinen, A. Howard, V. Ivanchenko, A. Johnson, F. Jones, J. Kallenbach, N. Kanaya, M. Kawabata, Y. Kawabata, M. Kawaguti, S. Kelner, P. Kent, A. Kimura, T. Kodama, R. Kokoulin, M. Kossov, H. Kurashige, E. Lamanna, T. Lampén, V. Lara, V. Lefebure, F. Lei, M. Liendl, W. Lockman, F. Longo, S. Magni, M. Maire, E. Medernach, K. Minamimoto, P. Mora de Freitas, Y. Morita, K. Murakami, M. Nagamatu, R. Nartallo, P. Nieminen, T. Nishimura, K. Ohtsubo, M. Okamura, S. O'Neale, Y. Oohata, K. Paech, J. Perl, A. Pfeiffer, M. Pia, F. Ranjard, A. Rybin, S. Sadilov, E. Di Salvo, G. Santin, T. Sasaki, N. Savvas, Y. Sawada, S. Scherer, S. Sei, V. Sirotenko, D. Smith, N. Starkov, H. Stoecker, J. Sulkimo, M. Takahata, S. Tanaka, E. Tcherniaev, E. Safai Tehrani, M. Tropeano, P. Truscott, H. Uno, L. Urban, P. Urban, M. Verderi, A. Walkden, W. Wander, H. Weber, J. Wellisch, T. Wenaus, D. Williams, D. Wright, T. Yamada, H. Yoshida, D. Zschiesche, Geant4—a simulation toolkit, Nucl. Instrum. Methods Phys. Res. A 506 (3) (2003) 250–303, http://dx.doi.org/10.1016/S0168-9002(03)01368-8, URL: https://linkinghub.elsevier.com/retrieve/pii/S0168900203013688.

[29] S. Kerhoas-Cavata, D. Guez, Modeling electronic processing in GATE, Nucl. Instrum. Methods Phys. Res. A 569 (2) (2006) 330–334, http://dx.doi.org/10.1016/j.nima.2006.08.107.

[30] E. Rault, S. Staelens, R. Van Holen, J. De Beenhouwer, S. Vandenberghe, Accurate Monte Carlo modelling of the back compartments of SPECT cameras, Phys. Med. Biol. 56 (1) (2011) 87–104, http://dx.doi.org/10.1088/0031-9155/56/1/006, URL: https://iopscience.iop.org/article/10.1088/0031-9155/56/1/006.

[31] F. Bataille, C. Comtat, S. Jan, R. Trebossen, Monte Carlo simulation for the ECAT HRRT using GATE, in: IEEE Symposium Conference Record Nuclear Science 2004, Vol. 4, 2004, pp. 2570–2574 Vol. 4, http://dx.doi.org/10.1109/NSSMIC.2004.1462778.

[32] S. Usman, A. Patil, Radiation detector deadtime and pile up: A review of the status of science, Nucl. Eng. Technol. 50 (7) (2018) 1006–1016, http://dx.doi.org/10.1016/j.net.2018.06.014, URL: https://linkinghub.elsevier.com/retrieve/pii/S1738573318302596.

[33] M. Yousaf, T. Akyurek, S. Usman, A comparison of traditional and hybrid radiation detector dead-time models and detector behavior, Prog. Nucl. Energy 83 (2015) 177–185, http://dx.doi.org/10.1016/j.pnucene.2015.03.018, URL: https://linkinghub.elsevier.com/retrieve/pii/S0149197015000839.

[34] W.-H. Wong, H. Li, J. Uribe, A high count rate position decoding and energy measuring method for nuclear cameras using Anger logic detectors, IEEE Trans. Nucl. Sci. 45 (3) (1998) 1122–1127, http://dx.doi.org/10.1109/23.681989, URL: http://ieeexplore.ieee.org/document/681989/.

[35] M. Conti, L. Eriksson, Physics of pure and non-pure positron emitters for PET: a review and a discussion, EJNMMI Phys. 3 (1) (2016) 8, http://dx.doi.org/10.1186/s40658-016-0144-5, URL: http://ejnmmiphys.springeropen.com/articles/10.1186/s40658-016-0144-5.

[36] A.N. Blacklocks, A.V. Chadwick, R.A. Jackson, K.B. Hutton, Investigation into thallium sites and defects in doped scintillation crystals, Phys. Status Solidi (C) 4 (3) (2007) 1008–1011, http://dx.doi.org/10.1002/pssc.200673704, URL: http://doi.wiley.com/10.1002/pssc.200673704.